Carbon 224 (2024) 119053

Contents lists available at ScienceDirect

Carbon

journal homepage: www.elsevier.com/locate/carbon

Membrane based *In-situ* reduction of graphene oxide for electrochemical supercapacitor application

Tongxi Lin [a], Xiaojun Ren [a], Xinyue Wen [a], Amir Karton [b,**], Vanesa Quintano [a,c,***], Rakesh Joshi [a,*]

[a] School of Materials Science and Engineering, University of New South Wales Sydney, NSW, 2052, Australia
[b] School of Science and Technology, University of New England, Armidale, NSW, 2351, Australia
[c] Catalan Institute of Nanoscience and Nanotechnology (ICN2), CSIC and BIST, Campus UAB, Bellaterra, 08193, Barcelona, Spain

ARTICLE INFO

Keywords:
Reduced graphene oxide
Vitamin C
Supercapacitor

ABSTRACT

Reduced graphene oxide (rGO) is a widely studied electrode material for energy storage, however, its strong re-stacking tendency during chemical reduction always leads to a degraded specific surface area and thus limits its performance. Therefore, it is necessary to control the morphology of rGO during the reduction process. Here, we develop a novel *in-situ* membrane-based method for the reduction of graphene oxide (GO) using a green and efficient vitamin C (VC) aqueous solution as reductant. The obtained electrode material (vitamin C reduced GO via membrane-based method, VG-M) exhibits a specific capacitance of 174 F/g at 1 A/g and 75.9% of retention at 40 A/g, which is about 9 times better than the highly self-stacked material from conventional methods (vitamin C reduced GO via stirring method, VG-S). This designed method successfully achieves the maintenance of rGO sheet morphology through laminar confinement in GO membrane and presents a simple approach towards two-dimensional (2D) material morphology control.

1. Introduction

Graphene oxide (GO) is a promising two-dimensional (2D) material with high specific surface area. As a graphene derivate, its carbon skeleton is decorated with oxygen functionalities, which largely limits its electrical conductivity and application in electrochemical energy storage, especially in supercapacitors. Therefore, reducing GO to produce reduced graphene oxide (rGO) has become a widely used method for obtaining high performance electrode materials with a high conductivity and large specific surface area [1]. Among the large number of methods to reduce graphene oxide, chemical reduction is one of the most investigated methods since it is simple, cost-effective and scalable [2]. However, chemical reduction of GO usually involves organic solvents and toxic reductants which are environmental friendly [3]. Recently, reducing GO with green and efficient reductant in aqueous solution has attracted many interests, and vitamin C (VC) is one of the most promising green reductants which is water soluble and can provide an efficiency as high as those conventional reductants [3]. With such favorable features, using VC to reduce GO may still cause some unfavorable changes of the materials that is similar to other chemical reduction methods, for example, the destruction of laminar structure and morphology.

Graphene oxide sheets tend to self-stack, and this self-stacking can be reopened by water molecules and the interlayer space can be accessible. However, in the reduction of GO, due to the removal of the hydrophilic oxygen functionalities, the self-stacked rGO sheets can hardly be separated again and thus it is difficult to recover the interlayer space [4]. Moreover, the increased in-plane strain caused by the removal of functionalities may lead to the self-folding of rGO sheets [5]. These unfavorable morphology changes will largely reduce the effective specific surface area of the materials and thus limit their performance [6]. Introducing surfactants or physical spacers is commonly performed to resist the self-stacking and aggregation of rGO materials during their synthesis [7]. However, these widely used approaches will inevitably associate with undesirable impurities which are usually difficult to be removed. Accordingly, we suggest that it will be more optimized if GO

* Corresponding author.
** Corresponding author.
*** Corresponding author. School of Materials Science and Engineering, University of New South Wales Sydney, NSW, 2052, Australia.
E-mail addresses: amir.karton@une.edu.au (A. Karton), v.quintano_ramos@unsw.edu.au (V. Quintano), r.joshi@unsw.edu.au (R. Joshi).

https://doi.org/10.1016/j.carbon.2024.119053
Received 31 January 2024; Received in revised form 4 March 2024; Accepted 16 March 2024
Available online 17 March 2024

can be reduced without undesirable chemical impurities or physical spacers while keeping its sheet morphology.

Herein, we propose a novel *in-situ* membrane-based method for reducing GO using a VC aqueous reductant. With the support of density functional theory (DFT) simulations, we first verified the feasibility of using VC to reduce GO and further revealed the reaction mechanism behind the high reactivity between VC and GO. The rGO membranes and materials were characterized with contact angle, X-ray photoelectron spectroscopy (XPS), Fourier transform infrared spectroscopy (FT-IR), X-ray diffraction (XRD), Raman spectroscopy, scanning electron microscopy (SEM), atomic force microscopy (AFM) and transmission electron microscopy (TEM). We thus suggested that with this novel method, GO sheets can be sufficiently reduced by VC under a highly laminate-confined environment in GO membrane (GOM) and largely remain their morphology.

2. Experimental

2.1. Materials

Polyvinylidene fluoride (PVDF) substrates (0.2 μm pore size, 25 mm and 47 mm diameters) were purchased from the Sterlitech Co. All the used chemicals including vitamin C (VC, L-ascorbic acid), Nafion (5 wt% dispersed in alcohols), H_2SO_4 (98%) and ethanol (99%) were purchased from Sigma-Aldrich Co.

2.2. GOM fabrication

GO solution is purchased from NiSiNa Materials Japan Co. The concentration of the obtained original GO suspension was 15 mg/mL, and then the original suspension was further diluted to 1 mg/mL stock concentration with de-ionized (DI) water. The fabrication of GOM was carried out with vacuum filtration. In a typical process, 2 mL of GO stock suspension (1 mg/mL) was added into a beaker and added DI water to 50 mL, then the diluted suspension was ultrasonicated for 10 min under ambient conditions. The obtained suspension was added into the vacuum filtration setup with a PVDF substrate (0.2 μm pore size, 47 mm diameter) and a pressure of about 0.9 bar. The loading mass of GO on PVDF substrate was 0.15 mg/cm^2 (effective area of PVDF coated by GO was 13.84 cm^2). The GOM fabrication process time was 4 h.

2.3. In-situ chemical reduction of GOMs

After the fabrication of GOM, 300 mL of VC aqueous solution with a VC content of 0 mg, 2 mg, 20 mg, 200 mg, 300 mg and 400 mg was very carefully added into the feed compartment of vacuum filtration setup, respectively. After the solution was completely filtrated out, the obtained VC reduced GOMs (VGMs) were dried in the air for 24 h. The samples were denoted according to their VC/GO mass ratio (e.g., VGM 200 stands for 400 mg of VC/2 mg of GO).

2.4. Preparation of rGO working electrodes

The fully reduced VGM 200 with a loading mass of 2 mg was soaked into 50 mL of DI water for 1 h and then ultrasonicated for 30 min to obtain the VC reduced GO material (VG-M) aqueous suspension. The VG-M samples were re-dispersed in ethanol to obtain a more homogeneous dispersion for more uniform electrode fabrication. For electrodes fabrication, the ink was prepared using 200 μL of VG-M suspension (1 mg/mL) mixing with 20 μL of Nafion ethanol solution (1 mg/mL) and ultrasonicated for 1 h. The ink was then drop-casted on strictly 1 cm^2 working area of a piece of 2 cm^2 carbon fiber paper. As prepared carbon paper was dried in an oven at 60 °C for 1 h to fabricate the working electrode. The VC reduced GO using conventional stirring method (VG-S) was prepared following a previously reported method for comparison [8], generally, 50 mg of VC was added to 50 mL of GO aqueous suspension (0.1 mg/mL) with vigorous stirring under ambient conditions for 48 h. The obtained VG-S aqueous suspension was vacuum filtrated, washed and dispersed in ethanol with a concentration of 1 mg/mL. The VG-S working electrode was fabricated with the same method as the VG-M working electrode. The active material loading mass of the working electrode was controlled to be around 0.2 mg by weighing before and after drop-casting.

2.5. Characterizations

The characterization of GOMs, VGMs, VG-M and VG-S samples were carried out using a range of analytical techniques. The surface hydrophobicity was measured by contact angle using the contact angle goniometer from Ossila. The VC concentration of the feed and permeate solutions was quantitatively analyzed by ultraviolet–visible spectrophotometer (UV–vis, PerkinElmer Lambda 365) with an external standard curve method. Field-emission scanning electron microscopy (FE-SEM, FEI Nova NanoSEM 230) was applied to characterize the surface morphology and cross-sectional structure of the synthesized materials and fabricated membranes. In addition to SEM, the topological information of GO sheets, VG-M and VG-S was also provided by atomic force microscopy (AFM, Bruker Dimension ICON SPM). Transmission electron microscopy (TEM, JEOL JEM-F200 Multi-Purpose FEG-S/TEM) was used to study the dimension of GO and VG-M sheets on lacey carbon grids. The X-ray diffraction (XRD) patterns were obtained to investigate the interlayer spacing (d-spacing) of the materials and membranes using PANalytical Empyrean I Thin-Film XRD at 45 kV 40 mA, and PANalytical MPD at 40 kV 40 mA with Cu Kα radiation ($\lambda = 0.154$ nm). The Fourier transform infrared spectroscopy (FT-IR) was characterized in ambient temperature with PerkinElmer Spectrum 100 spectrometer. The samples were scanned using universal attenuated total reflectance (ATR) mode from wavenumber of 650 cm^{-1} to 4000 cm^{-1} for obtaining the functional group information. The chemical composition was also investigated by an X-ray photoelectron spectrometer (XPS, Thermo ESCALAB250i) using a monochromatic Al Kalpha soft X-ray source for surface analysis and a monoatomic argon ion beam for depth profiling. Raman spectra were recorded from 1000 cm^{-1} to 3500 cm^{-1} on a Renishaw inVia Raman Microscope with 532 nm excitation laser.

2.6. Electrochemical measurements

All electrochemical measurements were carried out in three-electrode system using electrochemical workstation (WonATech Electrochemical Workstation ZIVE SP1) at ambient temperature. The prepared active material ink modified carbon fiber paper was used as working electrodes, an Ag/AgCl electrode with saturated KCl solution was used as reference electrode working with a platinum foil (2.5 cm × 2.5 cm) as counter electrode. 1 M H_2SO_4 solution was used as electrolyte of the cell. We performed several methods for measurements including cyclic voltammetry (CV), galvanostatic charge-discharge (GCD) and electrochemical impedance spectroscopy (EIS) to study the electrochemical profiles and supercapacitor performance of the fabricated working electrodes. The equations (eqn. 1 to eqn. 6) and detailed calculation are shown in **Supplementary note 1.** CV was performed from 10 mV/s to 1000 mV/s for VG-M and VG-S, and the capacitive contribution of VG-M was calculated through **SI 1 equation 1** [9]. GCD was performed from 1 A/g to 40 A/g for VG-M and VG-S, and the specific capacitance can be obtained from the discharging curves of GCD as **SI 1 equation 2** [10]. EIS was performed from 100 kHz to 10 mHz with an amplitude of 5 mV based on a stabilized open circuit potential (OCP). The dielectric relaxation time constant (τ_0) can be expressed by **SI 1 equation 3** [10]. The real part of complex capacitance and imaginary part of capacitance can be converted from the experimentally obtained impedance results from SI 1 equation 4–6 [10].

2.7. Computational methods

The density functional theory (DFT) calculations were performed at the PW6B95-D3BJ/def2-SVPP level of theory, carrying out geometries and harmonic vibrational frequencies of all structures [11,12]. Based on Becke–Johnson damping potential, Empirical D3 dispersion corrections are considered in the calculations [13,14]. Within such calculations, we obtained the Zero-point vibrational energies (ZPVEs), enthalpic temperature corrections (H_{298}–H_0) as well the entropic corrections. Real harmonic frequencies were verified at all equilibrium structures and only one imaginary frequency at the transition structures. The confirmation of connectivity of the transition and equilibrium structures was performed using intrinsic reaction coordinate (IRC) calculations [15]. The electronic energies were refined using the PWB95-D3BJ/def2-QZVPP level of theory [11,12]. CPCM continuum solvation model was used to include the bulk solvent effects in aqueous solution during calculations [16]. All calculations were obtained using the Gaussian 16 rev. C.01 program suite [17].

3. Results and discussion

3.1. Design of in-situ chemical reduction of GOMs

The widely used and studied well-aligned laminar structure of GOM [18–22] gave us an inspiration that confining GO sheets in GOM during reduction may maintain their morphology and resist the self-folding effect. Therefore, we designed an *in-situ* membrane-based GO reduction method using VC to obtain VC rGO membrane (VGM). The schematic of the designed synthesis process is illustrated in Fig. 1. The VC rGO material (VG-M) for electrochemical research was obtained by ultrasonicating sample VGM 200 due to its highest reduction degree. The reduction degree of the reduced GOMs were characterized via multiple techniques and will be analyzed and discussed below. It should be noted that VGM 200 is the highest reduced product we can obtain with this method, with higher VC content, the reduction degree of VGMs cannot reach higher level. For comparison, a previously reported conventional stirring method for reducing GO with VC was also performed to prepare VC rGO (VG-S). The sample photos and contact angle measurement results are shown in Fig. S1. Rejection tests were carried out to verify that VC molecules can pass through GOM and the results are shown in Fig. S2.

3.2. Computation of the VC-GO reaction mechanism

We carried out computational simulations to further understand the mechanism of VC-GO reduction. The mechanism of VC-GO reaction has been reported previously, where hydroxyl and epoxy groups on GO are mainly removed by VC [2,23–25], however, the detailed reaction processes are still unclear. Here, we performed density functional theory (DFT) calculations to gain insights into the mechanism of the reduction. These calculations were performed using the PW6B95-D3BJ exchange-correlation functional [26,27], which has been extensively benchmarked and found to provide excellent performance for both reaction energies and barrier heights [28–38]. For full computational details, see the **Supplementary note 2**. The Gibbs free potential energy surface (PES) in a simulated aqueous environment is shown in Fig. 2a–as well as the located local minima and each transition structure. Gibbs free reaction energies (ΔG_{298}) and barrier heights ($\Delta G^{\ddagger}_{298}$) are given relative to the separated VC and GO nanosheet with a single epoxy functional group (labeled as free reactants). We find that the reduction of the epoxy group proceeds via a multistep reaction mechanism, which involves two consecutive proton transfers associated with relatively low-lying transition structures. The barrier for the first proton transfer (TS1) is 54.2 kJ/mol relative to the free reactants, while that of the second proton transfer (TS2, can be considered as the reduction of hydroxyl group on GO) is 55.6 kJ/mol, which is practically barrierless relative to the intermediate complex (IC) formed in the first step (see Fig. 2a). Accordingly, there is no clear rate-determining step in this stepwise reaction mechanism. The final step is highly exergonic, which provides the entire reaction the thermodynamic driving force, also noticing the product complex shows dramatically lower energy as much as 173.1 kJ/mol than the free reactants. The computational results demonstrate that the reduction of GO with VC is a highly exergonic process associated with low-lying transition structures and will therefore proceed rapidly at room temperature.

3.3. Chemical composition

XPS and FT-IR were performed to understand the changes in chemical states during the reduction. The high resolution XPS C1s spectra of GOM, VGM 200 and VG-S are shown in Fig. 2b–d. The significantly declined C–O peaks (286.9 eV) in VGM 200 and VG-S indicate the removal of hydroxyl and epoxy groups after the VC-GO reaction [39,40]. The XPS survey spectra are shown in Figs. S3a–c, the C/O ratio of VGM 200 is 3.2 while the C/O ratio of VG-S is 4.6, the lower level of oxygen functionalities in VG-S indicates its higher reduction degree. The lower reduction degree of VGM 200 can be explained that compared to the free reduction environment of VG-S, the formation of GOM causes certain sites that are inaccessible for VC reduction. Additionally, the high resolution XPS O1s spectra of GOM, VGM 200 and VG-S are shown in Figs. S3d–f and detailed atomic percentages are shown in Table S1.

FT-IR spectra of samples with PVDF substrates and free-standing samples are shown in Fig. 2e and f respectively. The absorption bands at around 3195 cm^{-1}, 1725 cm^{-1}, 1620 cm^{-1}, 1390 cm^{-1}, 1220 cm^{-1} and 1050 cm^{-1} are attributed to -O-H in hydroxyl of GO and water, –C═O in carbonyl and carboxyl, sp^2-hybridized C═C, -O-H in carboxyl, alcohol and phenol, -C-O in epoxy and ether groups and -C-O in alkoxy and alkoxide, respectively [41–43]. Fig. 2e further supports the XPS results mentioned above, where compared to GOM, the hydroxyl and epoxy related peaks in VGM 200 and VG-S are reduced significantly. Particularly, the more decrease of -O-H peak at around 3195 cm^{-1} qualitatively implies that VG-S has a higher reduction degree than VGM 200. In order to better reveal the relationship between the VC addition (VC/GO mass ratio) and the functional group change without the interference from PVDF substrate, the GOM and VGMs were peeled off from the PVDF substrates to obtain free-standing samples, and then

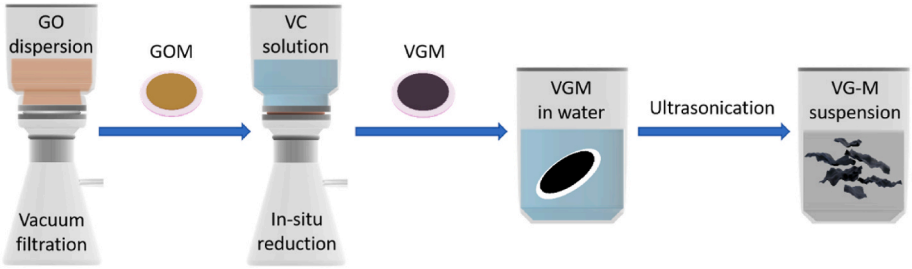

Fig. 1. Schematic illustration of the *in-situ* membrane-based reduction processes of GOM with VC.

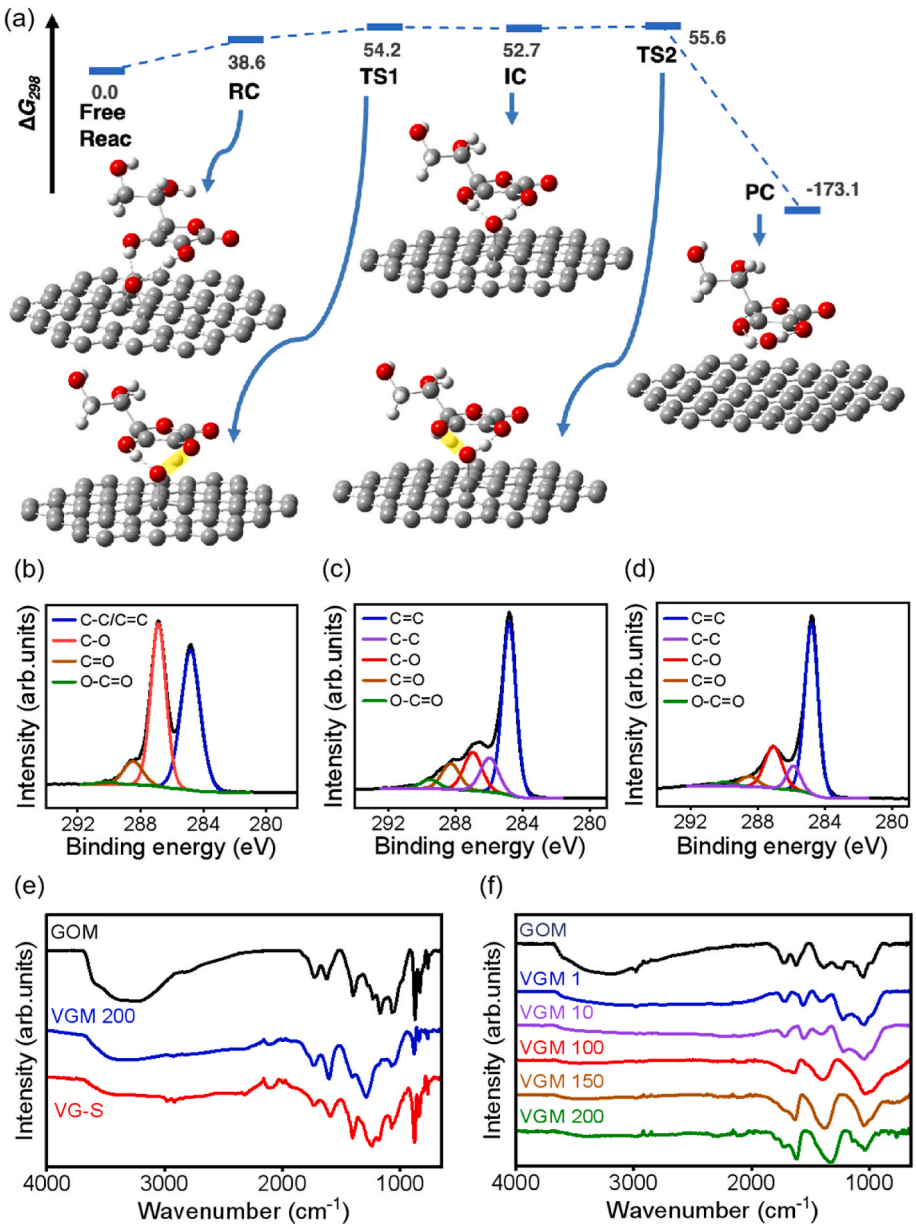

Fig. 2. DFT simulations of the reduction mechanism and chemical compositions of the materials. (a) Reaction profile (PW6B95-D3BJ/Def2-QZVPP, ΔG_{298}, kJ/mol) for the multistep reduction of a single epoxy group and hydroxyl group (second step) on the GO surface by VC in a simulated aqueous environment. The energies of the reactants, reactant complexes (RC), transition structures (TS1 and TS2), intermediate complex (IC), and product complex (PC) are given relative to the free reactants. The white, gray and red spheres represent H, C and O atoms, respectively. H-bonds are represented by white dashed lines, and the protons being transferred in the transition structures are highlighted in yellow. High resolution XPS C1s spectra of GOM (b), VGM 200 (c) and VG-S (d). (e) FT-IR spectra of GOM, VGM 200 and VG-S. (f) FT-IR spectra of GOM and VGMs.

characterized by FT-IR. Fig. 2f demonstrates that with the increase of VC/GO mass ratio, the intensities of -O-H peak (3195 cm^{-1}, hydroxyl group) and -C-O peak (1220 cm^{-1}, epoxy group) are gradually and obviously decreased. The observation of the decrease of -O-H peak and -C-O peak intensity confirms that the removal of hydroxyl and epoxy groups are the most significant reactions in VC-GO reaction, and these reactions can occur with a small addition of VC (at VC/GO mass ratio of 1). The results of XPS and FT-IR support the computational results we have demonstrated above that the predominant reaction mechanisms in VC-GO reaction are the removal of hydroxyl and epoxy groups on GO basal plane, and the reduction degree of VG-S in free reduction environment is higher than that of VGM 200, which is reduced in a confined laminar membrane.

3.4. *Material structure*

The structure of the materials was characterized by XRD and Raman spectroscopy. As shown in Fig. 3a, the original GOM shows a distinct (001) peak at 10.5° attributed to an 8.42 Å of interlayer space [21]. The strong intensity and sharp shape of the peak indicate the highly ordered laminar structure of GOM. With the increase of addition amount of VC, the (001) peaks of VGMs demonstrate a trend of shifting to a higher position and reducing their intensities, indicating the gradual decrease of the interlayer space due to the removal of oxygen functionalities on the GO basal plane. The changes of VGM (001) peaks are plotted and linear fitted with high agreement (Fig. 3b), indicating the high linear correlation between VC/GO mass ratio and the interlayer space in the VC *in-situ* reduction of GOM. In addition, the (001) peak is eliminated in

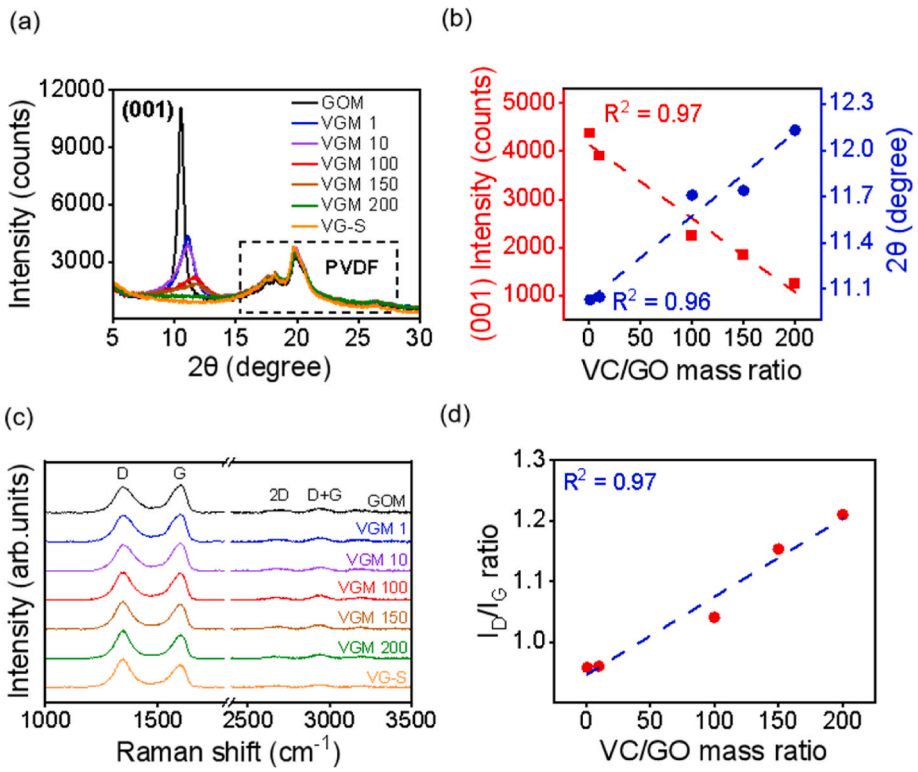

Fig. 3. Material structure characterizations of the membranes and materials. (a) XRD patterns of GOM, VGMs and VG-S on PVDF substrates. (b) The plot of (001) peak position and intensity vs. VC/GO mass ratio. (c) Raman spectra of GOM, VGMs and VG-S. (d) The plot of D/G ratio vs. VC/GO mass ratio.

the XRD pattern of VG-S, which represents the highest reduction degree was achieved in this study. Since the signal of (002) peak originated from the reduced GO interlayer space was covered by the signal of PVDF substrate (dashed box region in Fig. 3a), GOM and VGMs were carefully peeled off from the PVDF substrates and characterized by XRD to further understand the *in-situ* reduction process (Figs. S4a and b). In Fig. S4a, compared to Fig. 3a–a similar variation trend of (001) peak can be found. However, anomalously, in VGMs, with the decrease of (001) peak signal, the signal of (002) peak is not increased and even not obviously appeared (Fig. S4b), and only sample VGM 200 exhibits a broad (002) peak centered at around 21° (Fig. S4c). This gives a hint that the *in-situ* reduction may cause the disorder of the laminar alignment in the membrane due to the incomplete removal of functionalities on the GO basal plane.

Raman spectroscopy is a versatile technique for characterizing the material structure at a molecular level. D band (~1340 cm^{-1}) and G band (~1604 cm^{-1}) are the two mainly concerned regions in the Raman spectrum of GO and rGO materials (Fig. 3c), where D band corresponds to sp^3-hybridized carbons, edges and defects [44], and G band is related to the sp^2-hybridized carbons [45]. Additionally, a defect activated peak denoted as D + G mode can also be found at ~2920 cm^{-1} located in the 2D region [2]. The change of D/G ratio (I_D/I_G) were extracted from the Raman spectrum and plotted in Fig. S4d. The linear increase of VGM D/G ratio from 0.96 to 1.21 (Fig. 3d) indicates the highly corresponding relationship between the molecular disorder degree of the VGMs and the addition of VC (VC/GO mass ratio), where the higher (chemical) reduction degree causes more defects on rGO sheets. The increase of D/G ratio which represents the increase of defect ratio can be attributed to the mild reducing condition. Under ambient conditions, the reduction process will mainly remove hydroxyl and epoxy groups and restore C=C. It can be explained that a large number of double bonds were created, and only a relatively smaller number of defect-free graphitic domains were restored. Therefore, the increased D/G ratio can reasonably interpret that the reduction process statistically increases the total quantity of graphitic domains, but decreases the average size of sp^2 domains, especially the newly formed domains, and thus increase the fraction of edges and defects on rGO sheets [46].

3.5. Electrochemical performance

The electrochemical profile and supercapacitor material performance were evaluated to further understand the features of the VG-M material and explore its potential application. In order to evaluate the morphology influence on electrochemical profiles of VGM, we applied ultrasonication on VGM and using VG-M dispersion as the electrode material working in the three-electrode system rather than fabricating VGMs into a two-electrode system as reported in a previous study [47]. VG-M and VG-S working electrodes were fabricated via a simple drop-casting method (active material loading mass is ~0.2 mg) for electrochemical measurement in 1 M H_2SO_4 electrolyte (Fig. S5). Cyclic voltammetry (CV) was carried out to determine the electrochemical profiles of the fabricated electrodes. As shown in Fig. 4a, the CV curves of VG-M and VG-S at a scan rate of 100 mV/s both present as a nearly flawless rectangle within a pair of symmetric and broad redox. Such shape indicates their combined mechanism of electrical double-layer capacitance (EDLC) and pseudo-capacitance. The pseudo-capacitance behavior can be attributed to the Faradaic reactions introduced by the residual oxygen functionalities [48,49]. The CV curves with different scan rates are shown in Figs. S6a and b. The capacitive contribution of VG-M was calculated as ~75.8% at 100 mV/s (Fig. S6c) according to a kinetic calculation [9], which strongly supports its capacitance-controlled charge storage mechanism. Galvanostatic charge-discharge (GCD) was also performed to evaluate the performance of the materials (Figs. S6d–f). The capacitance performance and rate capability can thus be obtained via GCD. As shown in Fig. 4b, VG-M has a highest specific capacitance of 174 F/g at 1 A/g, and has a high retention of 75.9% at 40 A/g, while VG-S has a significantly lower capacitance of 19 F/g and a slightly higher retention at 40 A/g. Cycle

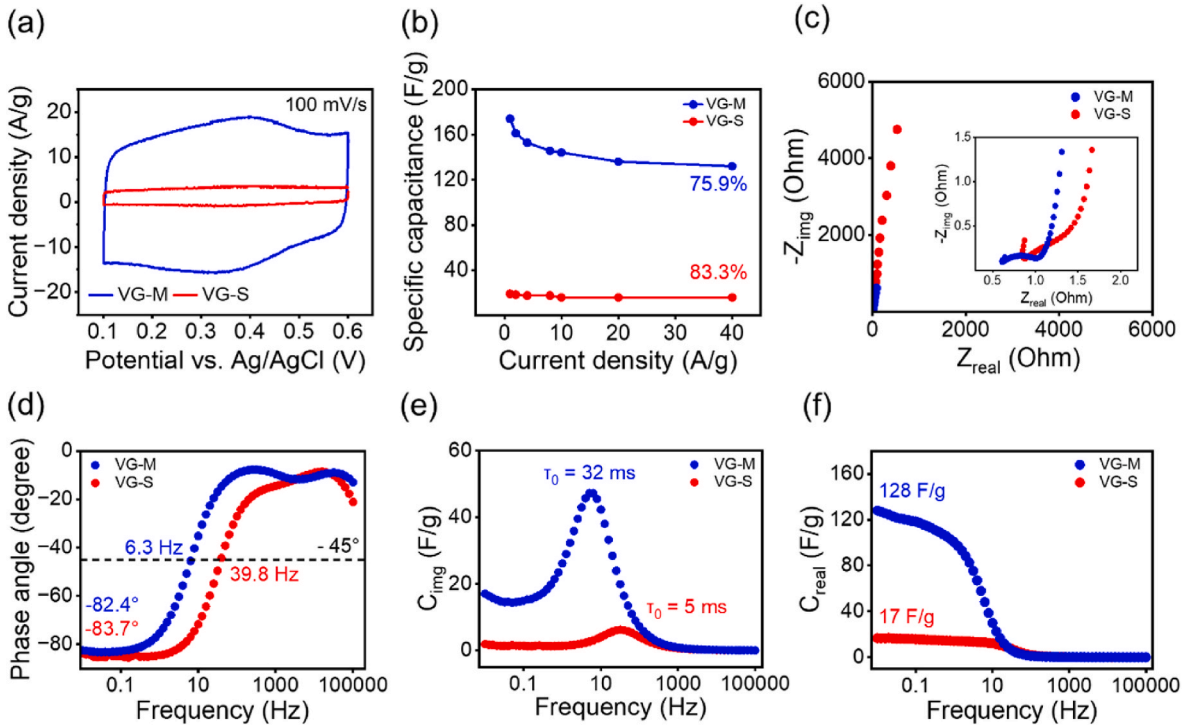

Fig. 4. Electrochemical profiles of VG-M and VG-S in 1 M H_2SO_4 in a three-electrode cell setup. (a) CV curves at a scan rate of 100 mV/s. (b) Rate capability study under various current densities from 1 A/g to 40 A/g. (c) Nyquist plots with an insert showing the magnified high frequency region. (d) Bode plots of phase angle vs. frequency. (e) Bode plots of imaginary capacitance vs. frequency. (f) Bode plots of real capacitance vs. frequency.

performance of VG-M was measured by applying GCD with a current density of 40 A/g, and a high retention of 93% can be achieved after 10, 000 cycles (Fig. S7).

In order to have a deeper insight into the electrochemical systems, electrochemical impedance spectroscopy (EIS) was applied from 100 kHz to 10 mHz with an amplitude of 5 mV based on a stabilized open circuit potential (OCP). The Nyquist plots are shown in Fig. 4c, both VG-M and VG-S feature nearly vertical curves in low frequency region, indicating their highly capacitive behaviors [48]. Meanwhile, in high frequency region, VG-M shows a smaller resistance than VG-S. VG-M samples have an equivalent series resistance (ESR) of 0.61 Ω and a charge transfer resistance (RCT) of 0.43 Ω, which are smaller than that of VG-S with 0.88 Ω and 0.65 Ω, respectively. Bode plots further reveal the frequency corresponding behaviors of the measured systems. As shown in Fig. 4d, VG-M and VG-S exhibit a phase angle of −82.4° and −83.7° respectively at 10 mHz, representing their nearly ideal capacitor behaviors (−90° at low frequency) [10]. In addition, a characteristic frequency (f_0) at the phase angle of −45° correlated to the peak frequency in the plot of imaginary capacitance (Fig. 4e) can also be extracted. Accordingly, a time constant can be calculated by $\tau_0 = 1/(2\pi f0)$ [10], where VG-S has a smaller τ_0 of 5 ms (39.8 Hz) than 32 ms of VG-M (6.3 Hz). This indicates that VG-S system has a faster ion migration and diffusion, and thus will have a better rate capability [50], which is supported by the GCD results. The real capacitance plot is shown in Fig. 4f, the real capacitances of VG-M and VG-S at 10 mHz are 128 F/g and 17 F/g, respectively. The low frequency value of real capacitance corresponds to pure EDLC, where most of the electrolyte ions can access deeply inside the material [51]. The much higher real capacitance of VG-M reveals that more electron-conductive sites in VG-M are available for electrolyte ions. By concluding the results, it is clear that VG-M has a significantly higher specific capacitance while VG-S performs better in rate capability. The similar electrochemical behaviors of the two materials indicate their same chemical nature. However, the obvious differences between VG-M and VG-S in performance and frequency-dependent behaviors are required to be further analyzed, and the mechanisms behind these features suggestively link to the morphology of the materials [6].

3.6. Morphology

The morphology of the samples was characterized by SEM, AFM and HRTEM. The cross-sectional (Fig. 5a–c) and surface (Figs. S8a, c, e) morphology of GOM, VGM and VG-S thick film on PVDF substrates were obtained from SEM. GOM shows a well-defined laminar cross-sectional feature and a smooth surface morphology. VGM 200 shows a roughly same cross-sectional and surface morphology with an increase of wrinkles. However, VG-S thick film exhibits a completely different morphology. The cross-section of VG-S can be defined as a thick film formed by stacking of fiber-like nanoparticles and the surface of VG-S presents a high degree of roughness and non-uniformity. In order to better understand the morphology of the materials that were used to fabricate the electrodes, VG-M, VG-S and GO (for comparison) were also characterized by SEM (Figs. S8b, d, f), and the results were in consistent with those of membranes and thick films, where GO can form a smooth and continuous surface via drop-casting, wrinkle-rich sheets can be found in VG-M sample, and severely aggregated fiber-like nanoparticles were observed in VG-S sample. The AFM topography shown in Fig. 5d–f provides detailed information of thickness and surface morphology of GO, VG-M and VG-S. Typically, GO sheets with a flat morphology and well-defined boundary can be found, and only a few continuous and smooth wrinkles exist on some of the sheets. Monolayer GO sheets with a height of ~1 nm can be discovered easily, which can be ascribed to the high hydrophilicity and dispersibility of GO. Significantly different from GO, the representative AFM image of VG-S shows a largely crumpled fiber-like particle with a length of 2 μm and width of 500 nm but with a height of more than 200 nm, which demonstrates its self-folded and aggregated features. Compared to VG-S, VG-M exhibits sheet features which are closer to GO sheets, however, presenting more homogeneously distributed wrinkles. Additional AFM images are shown in Fig. S9. In addition to AFM, HRTEM was also performed and images are

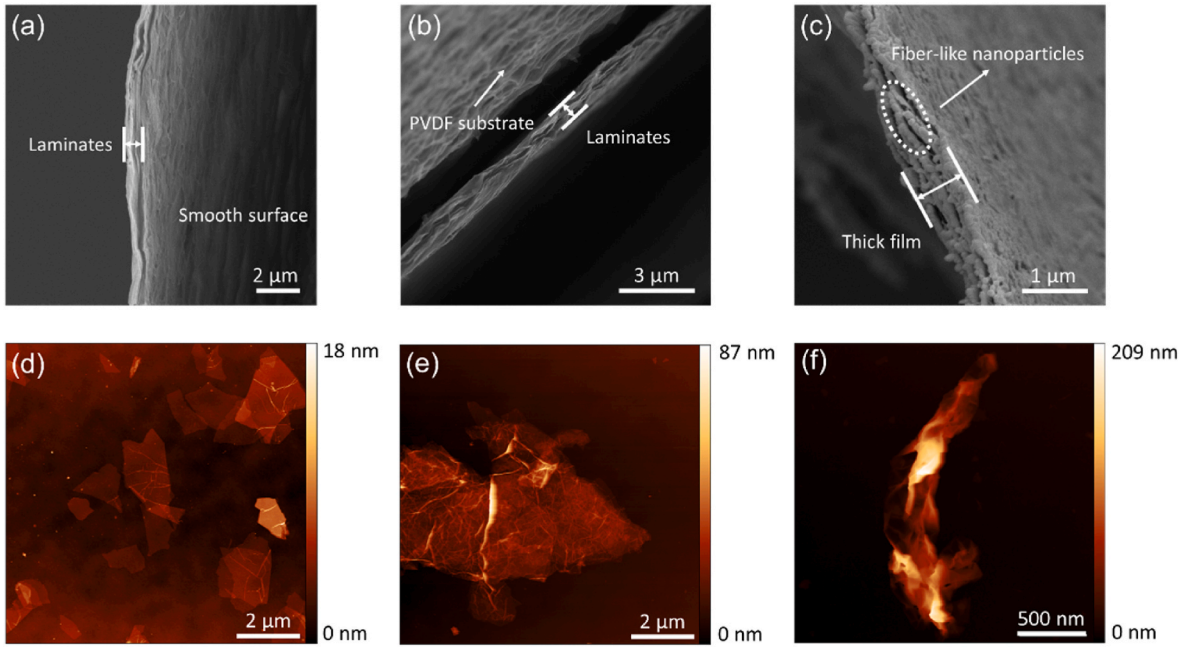

Fig. 5. Morphological characterizations of the membranes and materials. Cross-sectional SEM images of GOM (a), VGM 200 (b) and VG-S thick film (c). AFM images of GO (d), VG-M (e) and VG-S (f).

shown in Fig. S10.

3.7. Discussion

As mentioned above, the different charge storage performances and frequency-dependent behaviors of VG-M and VG-S may be suggestively related to the morphology. In order to clarify the influence of chemical functionalities on specific capacitance, as reported by a previous study, in 1 M H2SO4, the capacitance contribution of carbonyl group can be estimated as 13.55 F/g at%$^{-1}$. In our work, the XPS results show that the atomic percentage of C═O in VGM is 8.06 which is about 2 times higher than VG-S of 4.12. Therefore, based on the reported carbonyl group contribution, VG-M will theoretically have a specific capacitance of 54.2 F/g higher than VG-S due to higher carbonyl group content. However, we observed that VG-M has a specific capacitance of 174 F/g while VG-S has only 19 F/g. Considering the 54.2 F/g of specific capacitance which is attributed to the chemical functional group, VG-M still exhibits 119.8 F/g of specific capacitance which is 6.3 times higher than that of VG-S.

Beyond that, it is also reported that the reduction of rGO influences the supercapacitance of the material [52]. Lowering the reduction degree of rGO can indeed increases the specific capacitance, however, it will cause poor rate performance and stability. It is evident that increasing the reduction degree via chemical reduction (in a free environment) will cause the re-stacking of rGO and results in the decrease of its specific surface area and thus lower the specific capacitance [53]. Therefore, the higher supercapacitor performance of VG-M can be mainly attributed to the retained sheet morphology and the lower capacitance of VG-S may be attributed to the fiber-like morphology, which the self-folding caused by free reduction leads to the decrease of surface area. Due to the increase of hydrophobicity, electrolyte ions cannot access the depth of the particles. However, from a macroscopic perspective, the large pores created from the stacking of particles provide an ion diffusion path for high-speed ion migration, and thus improves the rate capability. As a contrast, VG-M with a sheet morphology achieves a much higher capacitance. This can be explained that the much thinner sheets improve the surface area where more electrolyte ions can access. In addition, the sheet-to-sheet attachment enables better connection for electron migration, and then activates more sheets to store charges. As a price, this better material connection and more compact material structure to some extent limit the ion diffusion channel and result in a slightly lower rate capability.

On the basis of the experimental results that we have analyzed and discussed above, the significant morphology difference between VG-S and VG-M is originated from their different reduction methods, and this morphology difference can be explained with the following hypothesis. VG-S is obtained from a conventional stirring method, where GO sheets are reduced by VC in a free environment. The rGO sheets are highly distorted in such a free environment due to the strong in-plane strain caused by the oxygen functionality removal [5,7], and thus form highly self-folded nanoparticles. More detailed morphology information can be observed by AFM peak force mode, as shown in Fig. S9. However, in the case of *in-situ* reduction of GOM, the GO sheets are restrictively confined by each other in a layer-by-layer stacked structure, where each GO sheet can be considered as a template and a confined material simultaneously. The high pressure (> 1 GPa) inside the interlayer of GO [54,55] is assumed to play a vital role in countering the in-plane strain caused by reduction. This laminar confinement phenomenon potentially keeps the near original GO laminar-membrane and sheet morphology of VGM and VG-M, respectively.

4. Conclusions

To summarize, we have demonstrated that an *in-situ* membrane-based GO reduction method using VC aqueous solution can largely retain the sheet morphology of rGO via laminar confinement. DFT simulations revealed that the mechanism toward the reduction of the epoxy and hydroxyl groups on GO by VC proceeds via low-lying transition structures and has a strong thermodynamic drive. Thus, these reductions are both kinetically and thermodynamically favorable. The VG-M material from our method exhibited much better supercapacitor performance than VG-S from conventional method in a free environment. Generally, for VG-M, a specific capacitance of 174 F/g can be obtained at 1 A/g and 75.9% of retention can be achieved at 40 A/g, which is about 9 times better than VG-S. The significant performance superiority of VG-M can be attributed to the retained sheet morphology

that provides more available sites for electrolyte ion storage. Compared to VG-S that is reduced in a free environment, VG-M is reduced in a highly confined environment, where the confinement counters the increased in-plane strain from reduction and thus maintains its original morphology. This study not only proposes a simple and promising process for producing a high-performance supercapacitor material but also provides a new insight for tuning the morphology of 2D materials.

CRediT authorship contribution statement

Tongxi Lin: Writing – original draft, Visualization, Validation, Methodology, Investigation, Formal analysis, Data curation, Conceptualization. **Xiaojun Ren:** Writing – review & editing, Visualization, Validation, Investigation, Data curation. **Xinyue Wen:** Writing – review & editing, Visualization, Investigation. **Amir Karton:** Writing – review & editing, Visualization, Validation, Investigation, Data curation. **Vanesa Quintano:** Writing – review & editing, Supervision, Investigation. **Rakesh Joshi:** Writing – review & editing, Validation, Supervision, Project administration, Investigation, Funding acquisition.

Declaration of competing interest

The authors declare that they have no known competing financial interests or personal relationships that could have appeared to influence the work reported in this paper.

Acknowledgement

Tongxi Lin acknowledges UNSW UIPA Scholarship. Vanesa Quintano acknowledges the funding from the European Union's Horizon 2020 research and innovation programme under the Marie Skłodowska Curie Grant Agreement No. 101066462. This work was undertaken with the assistance of resources from the National Computational Infrastructure (NCI), which is supported by the Australian Government. The authors thank Tobias Foller for discussion and acknowledge the support of Electron Microscope Unit (EMU), Spectroscopy Laboratory and Solid State & Elemental Analysis Unit (SSEAU) within the Mark Wainwright Analytical Centre (MWAC) at UNSW Sydney.

Appendix A. Supplementary data

Supplementary data to this article can be found online at https://doi.org/10.1016/j.carbon.2024.119053.

References

[1] M.F. El-Kady, Y. Shao, R.B. Kaner, Graphene for batteries, supercapacitors and beyond, Nat. Rev. Mater. 1 (2016) 16033, https://doi.org/10.1038/natrevmats.2016.33.
[2] K.K.H. De Silva, H.-H. Huang, R.K. Joshi, M. Yoshimura, Chemical reduction of graphene oxide using green reductants, Carbon N Y 119 (2017) 190–199, https://doi.org/10.1016/j.carbon.2017.04.025.
[3] M.J. Fernández-Merino, L. Guardia, J.I. Paredes, S. Villar-Rodil, P. Solís-Fernández, A. Martínez-Alonso, J.M.D. Tascón, Vitamin C is an ideal substitute for hydrazine in the reduction of graphene oxide suspensions, J. Phys. Chem. C 114 (2010) 6426–6432, https://doi.org/10.1021/jp100603h.
[4] H.-H. Huang, R.K. Joshi, K.K.H. De Silva, R. Badam, M. Yoshimura, Fabrication of reduced graphene oxide membranes for water desalination, J. Membr. Sci. 572 (2019) 12–19, https://doi.org/10.1016/j.memsci.2018.10.085.
[5] Y. Cao, Z. Xiong, F. Xia, G.V. Franks, L. Zu, X. Wang, Y. Hora, S. Mudie, Z. He, L. Qu, Y. Xing, D. Li, New structural insights into densely assembled reduced graphene oxide membranes, Adv. Funct. Mater. 32 (2022), https://doi.org/10.1002/adfm.202201535.
[6] J. Luo, H.D. Jang, J. Huang, Effect of sheet morphology on the scalability of graphene-based ultracapacitors, ACS Nano 7 (2013) 1464–1471, https://doi.org/10.1021/nn3052378.
[7] Y. Cao, Z. Xiong, Q. Liang, W.-J. Jiang, F. Xia, X. Du, L. Zu, S. Mudie, G.V. Franks, D. Li, Subnanometric stacking of two-dimensional nanomaterials: insights from the nanotexture evolution of dense reduced graphene oxide membranes, ACS Nano 17 (2023) 5072–5082, https://doi.org/10.1021/acsnano.3c00155.
[8] J. Zhang, H. Yang, G. Shen, P. Cheng, J. Zhang, S. Guo, Reduction of graphene oxide via <scp>l</scp> -ascorbic acid, Chem. Commun. 46 (2010) 1112–1114, https://doi.org/10.1039/B917705A.
[9] T. Brezesinski, J. Wang, S.H. Tolbert, B. Dunn, Ordered mesoporous α-MoO3 with iso-oriented nanocrystalline walls for thin-film pseudocapacitors, Nat. Mater. 9 (2010) 146–151, https://doi.org/10.1038/nmat2612.
[10] A. Noori, M.F. El-Kady, M.S. Rahmanifar, R.B. Kaner, M.F. Mousavi, Towards establishing standard performance metrics for batteries, supercapacitors and beyond, Chem. Soc. Rev. 48 (2019) 1272–1341, https://doi.org/10.1039/C8CS00581H.
[11] Y. Zhao, D.G. Truhlar, Design of density functionals that are broadly accurate for thermochemistry, thermochemical kinetics, and nonbonded interactions, J. Phys. Chem. A 109 (2005) 5656–5667, https://doi.org/10.1021/jp050536c.
[12] F. Weigend, R. Ahlrichs, Balanced basis sets of split valence, triple zeta valence and quadruple zeta valence quality for H to Rn: design and assessment of accuracy, Phys. Chem. Chem. Phys. 7 (2005) 3297, https://doi.org/10.1039/b508541a.
[13] S. Grimme, S. Ehrlich, L. Goerigk, Effect of the damping function in dispersion corrected density functional theory, J. Comput. Chem. 32 (2011) 1456–1465, https://doi.org/10.1002/jcc.21759.
[14] A.D. Becke, E.R. Johnson, A density-functional model of the dispersion interaction, J. Chem. Phys. 123 (2005), https://doi.org/10.1063/1.2065267.
[15] C. Gonzalez, H.B. Schlegel, An improved algorithm for reaction path following, J. Chem. Phys. 90 (1989) 2154–2161, https://doi.org/10.1063/1.456010.
[16] M. Cossi, N. Rega, G. Scalmani, V. Barone, Energies, structures, and electronic properties of molecules in solution with the C-PCM solvation model, J. Comput. Chem. 24 (2003) 669–681, https://doi.org/10.1002/jcc.10189.
[17] M.J. Frisch, G.W. Trucks, H.B. Schlegel, G.E. Scuseria, M.A. Robb, J.R. Cheeseman, G. Scalmani, V. Barone, G.A. Petersson, H. Nakatsuji, X. Li, M. Caricato, A. V Marenich, J. Bloino, B.G. Janesko, R. Gomperts, B. Mennucci, H.P. Hratchian, J. V Ortiz, A.F. Izmaylov, J.L. Sonnenberg, D. Williams-Young, F. Ding, F. Lipparini, F. Egidi, J. Goings, B. Peng, A. Petrone, T. Henderson, D. Ranasinghe, V. G. Zakrzewski, J. Gao, N. Rega, G. Zheng, W. Liang, M. Hada, M. Ehara, K. Toyota, R. Fukuda, J. Hasegawa, M. Ishida, T. Nakajima, Y. Honda, O. Kitao, H. Nakai, T. Vreven, K. Throssell, J.A. Montgomery Jr., J.E. Peralta, F. Ogliaro, M. J. Bearpark, J.J. Heyd, E.N. Brothers, K.N. Kudin, V.N. Staroverov, T.A. Keith, R. Kobayashi, J. Normand, K. Raghavachari, A.P. Rendell, J.C. Burant, S.S. Iyengar, J. Tomasi, M. Cossi, J.M. Millam, M. Klene, C. Adamo, R. Cammi, J.W. Ochterski, R.L. Martin, K. Morokuma, O. Farkas, J.B. Foresman, D.J. Fox, Gaussian~16 Revision C.01 (2016).
[18] X. Wen, T. Foller, X. Jin, T. Musso, P. Kumar, R. Joshi, Understanding water transport through graphene-based nanochannels via experimental control of slip length, Nat. Commun. 13 (2022) 5690, https://doi.org/10.1038/s41467-022-33456-w.
[19] X. Ren, D. Ji, X. Wen, H. Bustamante, R. Daiyan, T. Foller, Y.Y. Khine, R. Joshi, Graphene oxide membranes for effective removal of humic acid, J. Mater. Res. 37 (2022) 3362–3371, https://doi.org/10.1557/s43578-022-00647-6.
[20] T. Foller, X. Wen, Y.Y. Khine, D. Ji, T. Gupta, M. Muller, C. Scret, R. Joshi, Removal of chlorine and monochloramine from tap water using graphene oxide membranes, J. Membr. Sci. 686 (2023) 122022, https://doi.org/10.1016/j.memsci.2023.122022.
[21] R.K. Joshi, P. Carbone, F.C. Wang, V.G. Kravets, Y. Su, I.V. Grigorieva, H.A. Wu, A. K. Geim, R.R. Nair, Precise and ultrafast molecular sieving through graphene oxide membranes, Science 343 (2014) 752–754, https://doi.org/10.1126/science.1245711.
[22] T. Foller, L. Madauß, D. Ji, X. Ren, K.K.H. De Silva, T. Musso, M. Yoshimura, H. Lebius, A. Benyagoub, P.V. Kumar, M. Schleberger, R. Joshi, Mass transport via in-plane nanopores in graphene oxide membranes, Nano Lett. 22 (2022) 4941–4948, https://doi.org/10.1021/acs.nanolett.2c01615.
[23] K.K.H. De Silva, H.-H. Huang, M. Yoshimura, Progress of reduction of graphene oxide by ascorbic acid, Appl. Surf. Sci. 447 (2018) 338–346, https://doi.org/10.1016/j.apsusc.2018.03.243.
[24] M. Palomba, G. Carotenuto, A. Longo, A brief review: the use of L-ascorbic acid as a green reducing agent of graphene oxide, Materials 15 (2022) 6456, https://doi.org/10.3390/ma15186456.
[25] J. Gao, F. Liu, Y. Liu, N. Ma, Z. Wang, X. Zhang, Environment-friendly method to produce graphene that employs vitamin C and amino acid, Chem. Mater. 22 (2010) 2213–2218, https://doi.org/10.1021/cm902635j.
[26] Y. Zhao, D.G. Truhlar, Design of density functionals that are broadly accurate for thermochemistry, thermochemical kinetics, and nonbonded interactions, J. Phys. Chem. A 109 (2005) 5656–5667, https://doi.org/10.1021/jp050536c.
[27] S. Grimme, S. Ehrlich, L. Goerigk, Effect of the damping function in dispersion corrected density functional theory, J. Comput. Chem. 32 (2011) 1456–1465, https://doi.org/10.1002/jcc.21759.
[28] A. Karton, B. Chan, PAH335 – a diverse database of highly accurate CCSD(T) isomerization energies of 335 polycyclic aromatic hydrocarbons, Chem. Phys. Lett. 824 (2023) 140544, https://doi.org/10.1016/j.cplett.2023.140544.
[29] A.A. Kroeger, A. Karton, Catalysis by pure graphene—from supporting actor to protagonist through shape complementarity, J. Org. Chem. 84 (2019) 11343–11347, https://doi.org/10.1021/acs.joc.9b01909.
[30] A.A. Kroeger, A. Karton, π–π catalysis in carbon flatland—flipping [8]Annulene on graphene, Chem. Eur J. 27 (2021) 3420–3426, https://doi.org/10.1002/chem.202004045.
[31] L. Goerigk, A. Hansen, C. Bauer, S. Ehrlich, A. Najibi, S. Grimme, A look at the density functional theory zoo with the advanced GMTKN55 database for general main group thermochemistry, kinetics and noncovalent interactions, Phys. Chem. Chem. Phys. 19 (2017) 32184–32215, https://doi.org/10.1039/C7CP04913G.

[32] A. Karton, How reliable is DFT in predicting relative energies of polycyclic aromatic hydrocarbon isomers? comparison of functionals from different rungs of jacob's ladder, J. Comput. Chem. 38 (2017) 370–382, https://doi.org/10.1002/jcc.24669.
[33] L. Goerigk, R. Sharma, The INV24 test set: how well do quantum-chemical methods describe inversion and racemization barriers? Can. J. Chem. 94 (2016) 1133–1143, https://doi.org/10.1139/cjc-2016-0290.
[34] A. Karton, L. Goerigk, Accurate reaction barrier heights of pericyclic reactions: surprisingly large deviations for the <scp>CBS-QB3</scp> composite method and their consequences in <scp>DFT</scp> benchmark studies, J. Comput. Chem. 36 (2015) 622–632, https://doi.org/10.1002/jcc.23837.
[35] L. Goerigk, S. Grimme, A thorough benchmark of density functional methods for general main group thermochemistry, kinetics, and noncovalent interactions, Phys. Chem. Chem. Phys. 13 (2011) 6670, https://doi.org/10.1039/c0cp02984j.
[36] A. Karton, D. Gruzman, J.M.L. Martin, Benchmark thermochemistry of the C_nH_{2n+2} alkane isomers ($n = 2-8$) and performance of DFT and composite ab initio methods for dispersion-driven isomeric equilibria, J. Phys. Chem. A 113 (2009) 8434–8447, https://doi.org/10.1021/jp904369h.
[37] J. Zheng, Y. Zhao, D.G. Truhlar, The DBH24/08 database and its use to assess electronic structure model chemistries for chemical reaction barrier heights, J. Chem. Theor. Comput. 5 (2009) 808–821, https://doi.org/10.1021/ct800568m.
[38] A. Karton, A. Tarnopolsky, J.-F. Lamère, G.C. Schatz, J.M.L. Martin, Highly accurate first-principles benchmark data sets for the parametrization and validation of density functional and other approximate methods. Derivation of a robust, generally applicable, double-hybrid functional for thermochemistry and thermochemical kinetics, J. Phys. Chem. A 112 (2008) 12868–12886, https://doi.org/10.1021/jp801805p.
[39] R. Al-Gaashani, A. Najjar, Y. Zakaria, S. Mansour, M.A. Atieh, XPS and structural studies of high quality graphene oxide and reduced graphene oxide prepared by different chemical oxidation methods, Ceram. Int. 45 (2019) 14439–14448, https://doi.org/10.1016/j.ceramint.2019.04.165.
[40] Y.Y. Khine, X. Wen, X. Jin, T. Foller, R. Joshi, Functional groups in graphene oxide, Phys. Chem. Chem. Phys. 24 (2022) 26337–26355, https://doi.org/10.1039/D2CP04082D.
[41] Y.Y. Khine, X. Ren, D. Chu, Y. Nishina, T. Foller, R. Joshi, Surface functionalities of graphene oxide with varying flake size, Ind. Eng. Chem. Res. 61 (2022) 6531–6536, https://doi.org/10.1021/acs.iecr.2c00748.
[42] S. Park, K.-S. Lee, G. Bozoklu, W. Cai, S.T. Nguyen, R.S. Ruoff, Graphene oxide papers modified by divalent ions—enhancing mechanical properties *via* chemical cross-linking, ACS Nano 2 (2008) 572–578, https://doi.org/10.1021/nn700349a.
[43] L. Nie, K. Goh, Y. Wang, J. Lee, Y. Huang, H.E. Karahan, K. Zhou, M.D. Guiver, T.-H. Bae, Realizing small-flake graphene oxide membranes for ultrafast size-dependent organic solvent nanofiltration, Sci. Adv. 6 (2020), https://doi.org/10.1126/sciadv.aaz9184.
[44] A. Kaniyoor, S. Ramaprabhu, A Raman spectroscopic investigation of graphite oxide derived graphene, AIP Adv. 2 (2012), https://doi.org/10.1063/1.4756995.
[45] A.C. Ferrari, J.C. Meyer, V. Scardaci, C. Casiraghi, M. Lazzeri, F. Mauri, S. Piscanec, D. Jiang, K.S. Novoselov, S. Roth, A.K. Geim, Raman spectrum of graphene and graphene layers, Phys. Rev. Lett. 97 (2006) 187401, https://doi.org/10.1103/PhysRevLett.97.187401.
[46] Z. Bo, X. Shuai, S. Mao, H. Yang, J. Qian, J. Chen, J. Yan, K. Cen, Green preparation of reduced graphene oxide for sensing and energy storage applications, Sci. Rep. 4 (2014) 4684, https://doi.org/10.1038/srep04684.
[47] X. Yang, C. Cheng, Y. Wang, L. Qiu, D. Li, Liquid-mediated dense integration of graphene materials for compact capacitive energy storage, Science 341 (2013) 534–537, https://doi.org/10.1126/science.1239089.
[48] Y. Shao, M.F. El-Kady, C. Lin, G. Zhu, K.L. Marsh, J.Y. Hwang, Q. Zhang, Y. Li, H. Wang, R.B. Kaner, 3D freeze-casting of cellular graphene films for ultrahigh-power-density supercapacitors, Adv. Mater. 28 (2016) 6719–6726, https://doi.org/10.1002/adma.201506157.
[49] Z. Lin, Y. Liu, Y. Yao, O.J. Hildreth, Z. Li, K. Moon, C. Wong, Superior capacitance of functionalized graphene, J. Phys. Chem. C 115 (2011) 7120–7125, https://doi.org/10.1021/jp2007073.
[50] J. Chmiola, G. Yushin, R. Dash, Y. Gogotsi, Effect of pore size and surface area of carbide derived carbons on specific capacitance, J. Power Sources 158 (2006) 765–772, https://doi.org/10.1016/j.jpowsour.2005.09.008.
[51] P.L. Taberna, P. Simon, J.F. Fauvarque, Electrochemical characteristics and impedance spectroscopy studies of carbon-carbon supercapacitors, J. Electrochem. Soc. 150 (2003) A292, https://doi.org/10.1149/1.1543948.
[52] Y.J. Oh, J.J. Yoo, Y. Il Kim, J.K. Yoon, H.N. Yoon, J.-H. Kim, S. Bin Park, Oxygen functional groups and electrochemical capacitive behavior of incompletely reduced graphene oxides as a thin-film electrode of supercapacitor, Electrochim. Acta 116 (2014) 118–128, https://doi.org/10.1016/j.electacta.2013.11.040.
[53] S. Lin, J. Tang, K. Zhang, Y. Chen, R. Gao, H. Yin, L.-C. Qin, Tuning oxygen-containing functional groups of graphene for supercapacitors with high stability, Nanoscale Adv. 5 (2023) 1163–1171, https://doi.org/10.1039/D2NA00506A.
[54] D. Ji, Y. Lee, Y. Nishina, K. Kamiya, R. Daiyan, D. Chu, X. Wen, M. Yoshimura, P. Kumar, D.V. Andreeva, K.S. Novoselov, G. Lee, R. Joshi, T. Foller, Angstrom-confined electrochemical synthesis of sub-unit-cell non-van der waals 2D metal oxides, Adv. Mater. 35 (2023), https://doi.org/10.1002/adma.202301506.
[55] K.S. Vasu, E. Prestat, J. Abraham, J. Dix, R.J. Kashtiban, J. Beheshtian, J. Sloan, P. Carbone, M. Neek-Amal, S.J. Haigh, A.K. Geim, R.R. Nair, Van der Waals pressure and its effect on trapped interlayer molecules, Nat. Commun. 7 (2016) 12168, https://doi.org/10.1038/ncomms12168.